Numerical Simulation of Transient Inviscid Shock Tube Flows

J.Y. Yang*
NASA Ames Research Center, Moffett Field, California
C.K. Lombard†
PEDA Corporation, Palo Alto, California
and
D. Bershader‡
Stanford University, Stanford, California

Time-dependent upwind high resolution schemes for solving the Euler equations were developed and applied to simulate one- and two-dimensional transient inviscid gas flows in a shock tube. Using obstacles of different geometries, a series of calculations were carried out to investigate the transient complex shock wave diffraction phenomena. Shock wave and object interaction with shock Mach numbers ranging from 2–20 were simulated. Comparison with analytical and available experimental results indicate good agreement. Display of detailed flow structures including multiple Mach shocks, sliplines, and vortex are also given.

Introduction

In recent years a number of shock-capturing numerical techniques have been developed for solving the Euler equations of gas dynamics using upwind-difference methods. An excellent review on some of the recent developments in upwind-differencing schemes for hyperbolic conservation laws was given by Harten, Lax, and van Leer.[1] Meanwhile, several high-resolution, total variation-stable schemes using flux limiters[2] have been developed and applied to solve gas dynamical problems. Numerical experiments with these types of upwind schemes have experienced quite successful results for various situations of aerodynamic interest.

An extensive comparison of numerical methods for simulating two-dimensional gas dynamical flows with strong shocks has been given by Woodward and Collela.[3] Also, a class of explicit and implicit upwind flux-difference splitting schemes which have desirable shock-capturing capability have been developed by Lombard et al.[4,5] and Yang et al.[6-8] Application of implicit second-order upwind difference schemes to transonic flow problems were carried out in Refs. 7 and 8 and the numerical results indicate sharp shock representation with mainly one transition zone.

In this paper we apply one of the numerical schemes developed in Refs. 7 and 8 to simulate one- and two-dimensional unsteady flows of inviscid gas occuring in a shock tube, particularly for high-shock Mach number flows. A new approach for achieving second- and third-order spatial accuracy using a two-step procedure is also presented.

Our main purpose is to first establish a simple and robust second-order unsteady Euler code which is hopefully easier to implement than the classical Godunov method.[9,10] Second, simulating the transient shock-object interactions occuring in a shock tube and comparing them with experimental works and analytical results, we can assess the adequacy of the numerical algorithms used.

We mimic the real laboratory shock tube operation by starting the simulation at the moment when the diaphragm is broken; a single moving shock wave impinging on an obstacle can also be simulated. Various geometries including wedge and curved surfaces are considered and the nonstationary complex shock wave diffraction phenomena for a broad range of shock Mach number are studied.

There have been many experimental investigations of the shock wave propagation and interaction phenomena. They have produced both flowfield photographs and pressure-time histories of interaction, which not only explore the details of the flow structure but also provide means of comparing the accuracy of various theoretical and numerical approaches. Many of the works can be found in the *Proceedings of the International Symposium on Shock Tubes and Waves*.

On the other hand, there is also a need for time-accurate Euler codes for unsteady aerodynamic applications such as rotor aerodynamics, rocket ignition overpressure, and stability in solid-propellant rocket combustion. The present paper presents an initial effort to develop an unsteady Euler code to meet this task for flow with fixed solid surfaces and for flow with moving solid surfaces, such as in missile-launching application.

The numerical algorithms used are described in the following, as are two approaches to achieve second-order accuracy for a first-order monotonic scheme. Dimensional splitting was used for two-dimensional problems. Numerical calculation for one- and two-dimensional shock tube flows were carried out to test the present unsteady Euler code. Various geometries including compression wedge, concave and convex surfaces are considered, and comparison with analytical and available experimental works are made to assess the present numerical algorithms.

Euler Equations and Numerical Algorithms

We consider the two-dimensional Euler equations of gas dynamics in general curvilinear coordinate systems (ξ, η)

$$\partial_\tau Q + \partial_\xi F + \partial_\eta G = 0 \tag{1}$$

Presented as Papers 85-1679 at the AIAA 18th Fluid Dynamics, Plasmadynamics and Lasers Conference, Cincinnati, OH, July 16-18, 1985; received Aug 22, 1985.

*NRC Associate, Computational Fluid Dynamics Branch. Member AIAA.
†President. Member AIAA.
‡Professor, Department of Aeronautics and Astronautics.

where $Q = \boldsymbol{Q}/J$ and $F = (\xi_t \boldsymbol{Q} + \xi_x \boldsymbol{F} + \xi_y \boldsymbol{G})/J$, $G = (\eta_t \boldsymbol{Q} + \eta_x \boldsymbol{F} + \eta_y \boldsymbol{G})/J$, and $J = \xi_x \eta_y - \xi_y \eta_x$, is the metric Jacobian. $\boldsymbol{Q} = (\rho, \rho u, \rho v, e)^T$ is the conservative state vector, $\boldsymbol{F} = [\rho u, \rho u^2 + p, \rho uv, u(e+p)]^T$ and $\boldsymbol{G} = [\rho v, \rho vu, \rho v^2 + p, v(e+p)]^T$ are the flux vectors in Cartesian coordinates. Here ρ is the gas density, u, v are the gas velocity components, e the internal energy, and p the gas pressure. The pressure p is related to ρ, u, v, and e for an ideal gas by the following equation:

$$p = (\gamma - 1)\left[e - 0.5\rho(u^2 + v^2) \right] \tag{2}$$

where γ is the specific heats ratio.

Due to the hyperbolicity of Eq. (1), the Jacobian coefficient matrix $A_\xi = \partial F/\partial Q$ of the transformed equations has real eigenvalues U, $U + c_\xi$, U, and $U - c_\xi$, where $U = \xi_t + \xi_x u + \xi_y v$, and $c_\xi = c(\xi_x^2 + \xi_y^2)^{1/2}$, where $c = (\gamma p/\rho)^{1/2}$ is the speed of sound. [Similarly, the eigenvalues of $B_\eta = \partial G/\partial Q$ are $V, V, V + c_\eta$, and $V - c_\eta$, with $V = \eta_t + \eta_x u + \eta_y v$, and $c_\eta = c(\eta_x^2 + \eta_y^2)^{1/2}$.]

One can find similarity transformation matrices T_ξ and T_η such that

$$T_\xi^{-1} M^{-1} A_\xi M T_\xi = \Lambda_\xi \qquad T_\eta^{-1} M^{-1} B_\eta M T_\eta = \Lambda_\eta \tag{3}$$

In Eq. (3), $M = \partial \boldsymbol{Q}/\partial \boldsymbol{Q}^p$ is the transformation between conservative variables and the primitive variables $\boldsymbol{Q}^p = (\rho, u, v, p)^T$, and Λ_ξ and Λ_η are diagonal matrices

$$\Lambda_\xi = \text{diag}\{ a_\ell \} \quad \text{and} \quad \Lambda_\eta = \text{diag}\{ b_\ell \} \tag{4}$$

where a_ℓ, and b_ℓ, $\ell = 1, \ldots, 4$ are eigenvalues of A_ξ and B_η respectively.

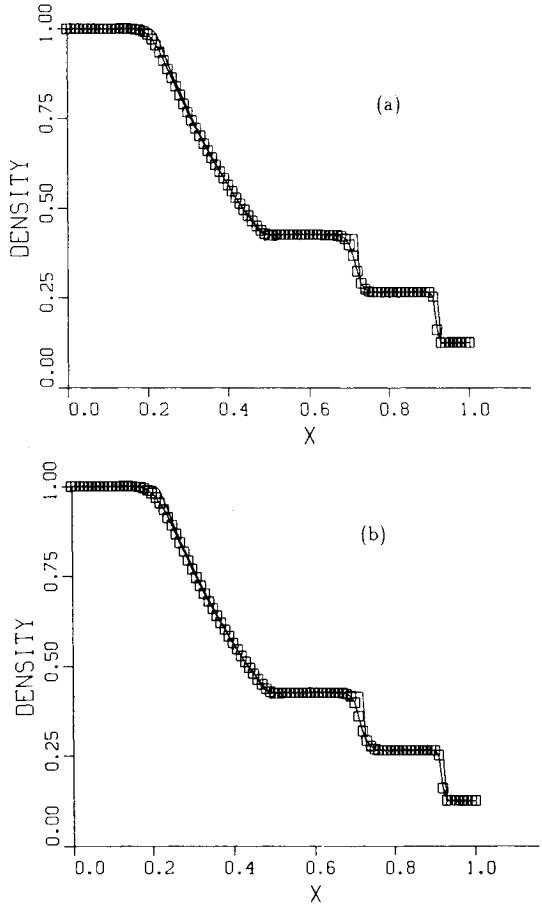

Fig. 1 Solution of one-dimensional shock tube: a) scheme II with $\kappa = 0$, b) scheme II with $\kappa = 1/3$.

Applying the characteristic flux-difference splitting method[6-8] to Eq. (1) we have

$$\partial_\tau Q + \left(\boldsymbol{A}_\xi^+ + \boldsymbol{A}_\xi^- \right) \partial_\xi F + \left(\boldsymbol{B}_\eta^+ + \boldsymbol{B}_\eta^- \right) \partial_\eta G = 0 \tag{5}$$

where the "normalized" Jacobian coefficient matrices $\boldsymbol{A}_\xi^\pm$ and $\boldsymbol{B}_\eta^\pm$ are closedly related to A_ξ and B_η through the following definition:

$$\boldsymbol{A}_\xi^\pm = M T_\xi \Lambda_\xi^\pm T_\xi^{-1} M^{-1} \qquad \boldsymbol{B}_\eta^\pm = M T_\eta \Lambda_\eta^\pm T_\eta^{-1} M^{-1} \tag{6}$$

The normalized diagonal matrices $\Lambda_\xi^\pm$ and $\Lambda_\eta^\pm$ are given by

$$\Lambda_\xi^\pm = \text{diag}\{ \boldsymbol{a}_\ell^\pm \} \quad \text{and} \quad \Lambda_\eta^\pm = \text{diag}\{ \boldsymbol{b}_\ell^\pm \} \tag{7}$$

where

$$\boldsymbol{a}_\ell^\pm = \frac{1 \pm \text{sgn}(a_\ell)}{2} \quad \text{and} \quad \boldsymbol{b}_\ell^\pm = \frac{1 \pm \text{sgn}(b_\ell)}{2} \tag{8}$$

Explicit time-splitting is employed subsequently for solving Eq. (5). In this way the solution procedure becomes locally one-dimensional and can be represented as

$$Q_{j,k}^{n+2} = L_\xi(\Delta\tau) L_\eta(\Delta\tau) L_\eta(\Delta\tau) L_\xi(\Delta\tau) Q_{j,k}^n \tag{9}$$

For the L_ξ operator in the ξ direction, we have

$$L_\xi Q_{j,k}^n = Q_{j,k}^* = Q_{j,k}^n - \lambda_\xi \left(F_{j+\frac{1}{2},k}^N - F_{j-\frac{1}{2},k}^N \right) \tag{10}$$

where $\lambda_\xi = \Delta\tau/\Delta\xi$ and $F_{j+\frac{1}{2},k}^N$ is the numerical flux, which for the first-order scheme is given by

$$F_{j+\frac{1}{2},k}^N = F_{j+1,k}^n - (\Delta F)_{j+\frac{1}{2},k}^+ = F_{j,k}^n + (\Delta F)_{j+\frac{1}{2},k}^- \tag{11}$$

with

$$(\Delta F)_{j+\frac{1}{2},k}^\pm = \boldsymbol{A}_{\xi_{j+\frac{1}{2},k}}^\pm \Delta_{j+\frac{1}{2},k} F^n \tag{12}$$

$$\Delta_{j+\frac{1}{2},k} F^n = (\Delta F)_{j+\frac{1}{2},k}^+ + (\Delta F)_{j+\frac{1}{2},k}^- = F_{j+1,k}^n - F_{j,k}^n \tag{13}$$

The L_η operator in the η direction is written as

$$L_\eta Q_{j,k}^* = Q_{j,k}^{n+1} = Q_{j,k}^* - \lambda_\eta \left[G_{j,k+\frac{1}{2}}^{*N} - G_{j,k-\frac{1}{2}}^{*N} \right] \tag{14}$$

The numerical flux $G_{j,k+\frac{1}{2}}^{*N}$ can be similarly given.

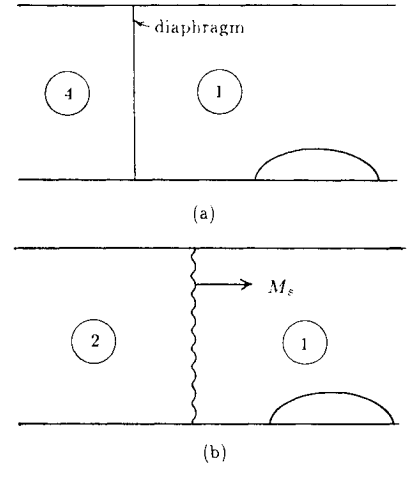

Fig. 2 Schematic diagram of a shock tube: a) with diaphragm, b) with single moving shock.

Several approaches can be taken to achieve second- or higher-order accuracy and total variation stable (see Ref. 7 and the references sited therein). One approach is to use a more accurate representation of the flux vectors, such as the modified-flux approach deviced by Harten.[11] Another is to use a more accurate representation of the initial distribution of the Q conservative variables, such as the MUSCL approach advanced by van Leer.[12,13] Additionally, another approach is to use characteristic interpolation with the Lagrangian formula.[8]

In the following section, a second-order scheme will be described using a more accurate representation of the flux vector in which we closely follow the modified-flux approach of Harten. A scheme using van Leer's MUSCL approach is also described. Both approaches are cast into the framework of characteristic flux-difference splitting.[6]

Scheme I. Modified Flux Approach

In Ref. 11, Harten has described a recipe for converting a three-point first-order upwind-difference scheme to a five-point TVD scheme. Here we adopt his approach and extend it to the framework of characteristic flux difference splitting.

First, a modified flux vector is defined for a hyperbolic system of conservation laws based on the characteristic flux-difference splitting concept. Then applying our first-order scheme to this modified-flux vector, we solve

$$\partial_\tau Q + \left(A_\xi^+ + A_\xi^-\right)\partial_\xi F^M + \left(B_\eta^+ + B_\eta^-\right)\partial_\eta G^M = 0 \quad (15)$$

where F^M and G^M are the modified flux vectors. The value of F^M at nodal point j,k is given by

$$F^M_{j,k} = F^n_{j,k} + E_{j,k}/\lambda_\xi \quad (16)$$

where F is the original flux vector and E is an additional vector remaining to be defined. The column vector E at nodal point j,k is $E_{j,k} = (e_1, e_2, e_3, e_4)^T_{j,k}$ and its ℓ component is given by

$$\begin{aligned} e_{\ell_{j,k}} &= 0, \qquad \text{if } \tilde{e}_{\ell_{j+\frac{1}{2},k}}\tilde{e}_{\ell_{j-\frac{1}{2},k}} \le 0 \\ &= s_{\ell_{j+\frac{1}{2},k}} \min\left(|\tilde{e}_{\ell_{j+\frac{1}{2},k}}|, |\tilde{e}_{\ell_{j-\frac{1}{2},k}}|\right), \qquad \text{otherwise} \end{aligned} \quad (17)$$

where $\tilde{e}_{\ell_{j+\frac{1}{2},k}}$ ($\ell = 1,2,3,4$) are components of the following column vector:

$$\tilde{E}_{j+\frac{1}{2},k} = \left(\lambda_\xi/2\right)\operatorname{sgn} A_{\xi_{j+\frac{1}{2},k}}\left(I - \lambda_\xi |A_{\xi_{j+\frac{1}{2},k}}|\right)\Delta_{j+\frac{1}{2},k} F \quad (18)$$

and

$$s_{\ell_{j+\frac{1}{2},k}} = \operatorname{sgn}\left(\tilde{e}_{\ell_{j+\frac{1}{2},k}}\right) \quad (19)$$

The sgn A_ξ in Eq. (18) is given by

$$\operatorname{sgn} A_\xi = M T_\xi \operatorname{diag}\{\operatorname{sgn} a_\ell\} T_\xi^{-1} M^{-1} \quad (20)$$

The second-order accuracy comes from the second term of Eq. (18).

A second-order accurate TVD scheme based on Eq. (15), solved in time-splitting fashion as Eq. (9), and expressed in terms of numerical flux F^N is

$$F^N_{j+\frac{1}{2},k} = F^M_{j+1,k} - A^+_{\xi_{j+\frac{1}{2},k}}\Delta_{j+\frac{1}{2},k} F^M = F^M_{j,k} + A_{\xi_{j+\frac{1}{2},k}}\Delta_{j+\frac{1}{2},k} F^M \quad (21)$$

Similar expression can be given for the L_η operator.

Scheme II. MUSCL-Type Approach

In the following, we describe an explicit scheme using MUSCL-type approach advanced by van Leer[13] and employed by Anderson et al.[14]

For illustration purposes, we use the one-dimensional Euler equation

$$\partial_t Q + \partial_x F(Q) = 0 \quad (22)$$

In this approach, one first extrapolates nodal-point values of Q toward the cell interfaces as:

$$Q^-_{j+\frac{1}{2}} = Q_j + \left(S_j/4\right)\left[\left(I - \kappa S_j\right)\Delta_{-j} + \left(I + \kappa S_j\right)\Delta_{+j}\right] \quad (23a)$$

$$Q^+_{j-\frac{1}{2}} = Q_j - \left(S_j/4\right)\left[\left(I - \kappa S_j\right)\Delta_{+j} + \left(I + \kappa S_j\right)\Delta_{-j}\right] \quad (23b)$$

where $\Delta_{\pm j} = \pm(Q_{j\pm1} - Q_j)$ and $S_j = \operatorname{diag}\{s_{\ell,j}\}$ is a diagonal matrix with its element given by

$$s_{\ell,j} = \frac{2\delta_{+\ell,j}\delta_{-\ell,j} + \epsilon}{\left(\delta_{+\ell,j}\right)^2 + \left(\delta_{-\ell,j}\right)^2 + \epsilon} \quad (24)$$

where $\delta_{+\ell,j}$ and $\delta_{-\ell,j}$ are components of Δ_{+j} and Δ_{-j}, respectively, and $\epsilon \approx (\Delta x^3)$.

Then one advances $Q^{\mp}_{j\pm\frac{1}{2}}$ to $t^{n+\frac{1}{2}}$ as follows:

$$Q^{*\mp}_{j\pm\frac{1}{2}} = Q^{\mp}_{j\pm\frac{1}{2}} - \frac{\Delta t}{2\Delta x}\left[F\left(Q^-_{j+\frac{1}{2}}\right) - F\left(Q^+_{j-\frac{1}{2}}\right)\right] \quad (25)$$

The final scheme is given as

$$Q^{n+1}_j = Q^n_j - \frac{\Delta t}{\Delta x}\left[F^N\left(Q^{*-}_{j+\frac{1}{2}}, Q^{*+}_{j+\frac{1}{2}}\right) - F^N\left(Q^{*-}_{j-\frac{1}{2}}, Q^{*+}_{j-\frac{1}{2}}\right)\right] \quad (26)$$

with the numerical flux, again, given by the characteristic flux difference splitting

$$\begin{aligned} &F^N\left(Q^{*-}_{j+\frac{1}{2}}, Q^{*+}_{j+\frac{1}{2}}\right) \\ &\quad = F\left(Q^{*+}_{j+\frac{1}{2}}\right) - A^+_{j+\frac{1}{2}}\left[F\left(Q^{*+}_{j+\frac{1}{2}}\right) - F\left(Q^{*-}_{j+\frac{1}{2}}\right)\right] \\ &\quad = F\left(Q^{*-}_{j+\frac{1}{2}}\right) + A^-_{j+\frac{1}{2}}\left[F\left(Q^{*+}_{j+\frac{1}{2}}\right) - F\left(Q^{*-}_{j+\frac{1}{2}}\right)\right] \end{aligned} \quad (27)$$

For $S_j = 0$, one has a first-order scheme exactly the same as Eq. (11). For $\kappa = 0$, we have second-order spatial accuracy and for $\kappa = \frac{1}{3}$, we have third-order spatial accuracy.

Boundary Conditions

In this section the boundary conditions employed are described. Equations (10) and (14) are for the interior points. At the boundary points, i.e., inflow ($j = 1$) and outflow ($j = J$) boundaries, lower ($k = 1$) and upper ($k = K$) surfaces, the following boundary point schemes were used.

At the lower surface, $k = 1$

$$Q^*_{j,1} = Q^n_{j,1} - \lambda_\eta B^-_{j,\frac{3}{2}}\left(G_{j,2} - G_{j,1}\right) \quad (28a)$$

and at the upper surface, $k = K$

$$Q^*_{j,K} = Q^n_{j,K} - \lambda_\eta B^+_{j,K-\frac{1}{2}}\left(G_{j,K} - G_{j,K-1}\right) \quad (28b)$$

At the lower surface, the information comes from the right-running characteristics associated with the eigenvalue $b_3 = V + c_\eta$ and can not be properly accounted by Eq. (28a). Additional conditions are needed to supplement Eq. (28a) in order to update the state variables Q on the surface $k = 1$;

these are furnished by the Riemann invariants corresponding to this characteristic, b_3. They are

$$V_\eta^{n+1} - (2c^{n+1})/(\gamma - 1) = V_\eta^* - (2c^*)/(\gamma - 1) \quad (29a)$$

$$p^{n+1}/(\rho^{n+1})^\gamma = p^*/(\rho^*)^\gamma \quad (29b)$$

$$V_\xi^{n+1} = V_\xi^* \quad (29c)$$

and together with the surface tangency condition

$$V_\eta^{n+1} = 0 \quad (29d)$$

where $V_\eta = V/|\nabla_\eta|$ and $V_\xi = (\eta_y u - \eta_x v)/|\nabla_\eta|$.

Equation (29) gives the four equations to solve for the state variables $Q_{j,1}^{n+1}$ at the new time level. A similar procedure can be employed for the upper surface.

Results and Discussions

In this section we present some calculations and results using the second-order upwind-difference schemes which we have described previously.

Several geometries are considered in this study. They are 1) one-dimensional shock tube, 2) 15%-thick circular arc convex surface, 3) 30 deg compression ramp, and 4) a 90 deg bent duct. Cases 2–4 are two-dimensional problems. Brief descriptions of each case is given subsequently.

One-Dimensional Shock Tube Flows

The first result is a simple one-dimensional shock tube problem. The initial condition is given by

$$p_L = 1, \quad \rho_L = 1, \quad u_L = 0, \quad 0 \le x \le 0.5$$

$$p_R = 0.1, \quad \rho_R = 0.125, \quad u_R = 0, \quad 0.5 \le x \le 1$$

This problem is solved mainly to test the numerical schemes and to establish the adequacy of the current approach. Comparison with other methods has been made in Ref. 6. All calculations are done using a uniform grid with $\Delta x = 0.01$ and $\Delta t = 0.4\Delta x$. The results were plotted after 60 integration steps.

Figure 1 shows the density profile of a one-dimensional shock tube problem using scheme II with $\kappa = 0$ and $\kappa = \frac{1}{3}$, respectively. The solid connecting line is the analytical solution and the boxes are the computed solutions. The results show sharp shock capturing capability and the contact surface is reasonably resolved. For scheme II, we found almost identical results for $\kappa = 0$ and $\kappa = \frac{1}{3}$. In this study, scheme II is applied only to one-dimensional problems. For extension to multi-dimensional problems, rotational formulation can be incorporated.[14]

Two-Dimensional Shock Tube Flows

The second result we present is the simulation of shock passing a 15%-thick circular arc model. The schematical diagram of a two-dimensional shock tube is depicted in Fig. 2. The initial gas states on both sides of the diaphragm are selected such that a shock moving with $M_s = 2$ is generated. The basic equation for shock tube is given by

$$\frac{p_4}{p_1} = \frac{2\gamma M_s^2 - (\gamma - 1)}{\gamma + 1}\left[1 - \frac{\gamma - 1}{\gamma + 1}\left(M_s - \frac{1}{M_s}\right)\right]^{-(2\gamma)/(\gamma-1)} \quad (30)$$

In Eq. (30) we choose $\gamma_1 = \gamma_4 = \gamma = 1.4$ and $c_1/c_4 = 1$. The initial conditions are

$$u_4 = 0, \; v_4 = 0, \; \rho_4 = 1; \qquad u_1 = 0, \; v_1 = 0, \; p_1 = 1$$

The pressure p_4 is obtained from the shock tube equation. For $M_s = 2$, we have $p_4/p_1 = 33.712$.

We also consider a single moving shock impinging on a model. The condition ahead of and behind a moving shock are

$$p_2/p_1 = [2\gamma M_s^2 - (\gamma - 1)]/(\gamma + 1) \quad (31a)$$

$$\rho_2/\rho_1 = [\Gamma(p_2/p_2) + 1]/[\Gamma + (p_2/p_1)] \quad (31b)$$

$$u_2 = M_s\{1 - [(\gamma - 1)M_s^2 + 2]/[(\gamma + 1)M_s^2]\}\, c_1 \quad (31c)$$

where $\Gamma = (\gamma + 1)/(\gamma - 1)$ and $c_1 = (\gamma p_1/\rho_1)^{1/2}$.

Figure 3a shows the pressure contour for a shock tube flow with primary shock Mach number $M_s = 2$ passing a 15% circular arc. The primary shock, the reflected shock, and the vortex are well captured and reasonably resolved. Also, reflection shock starts to hit the upper surface and is being reflected back. (cf. all calculations are done using $CFL = 0.9$.)

Results of a single moving shock impinging on the circular arc are shown in Fig. 3b. Again, the physical structures is well presented. The difference between the two cases are the reflected shock is further compressed by the right-running contact surface.

In order to compare with experimental works and compare with other numerical simulations we also consider the case of a unsteady shock wave with Mach number $M_s = 5.29$ passing a 30 deg compression corner. The experimental results are from Ben-Dor and Glass[16] and Deschambault and Glass.[17]

For this planar wedge problem, it was observed experimentally and predicted theoretically that the two shock configurations at a wedge grow with time in a self-similar fashion. The process is called pseudo-steady. The value of γ is taken to be 5/3 for a perfect monatomic gas.

Figures 4a and 4b display the isopycnics and pressue contours. Density distribution on the wedge surface is shown in Fig. 4c, and the experimental result from Ref. 16 is shown in Fig. 4d.

Comparison with Figs. 15c and 16c of Ref. 16 and Figs. 16c and 17 of Ref. 17, indicate that the present results are in good agreement with the experimental works. A more refined grid seems to be necessary in order to resolve the triple shock and the slipline.

Figures 5a and 5b display density and pressure contours for shock with $M_s = 6$ propagating along a 90 deg bent in a two-dimensional duct. The flow patterns around the bend are

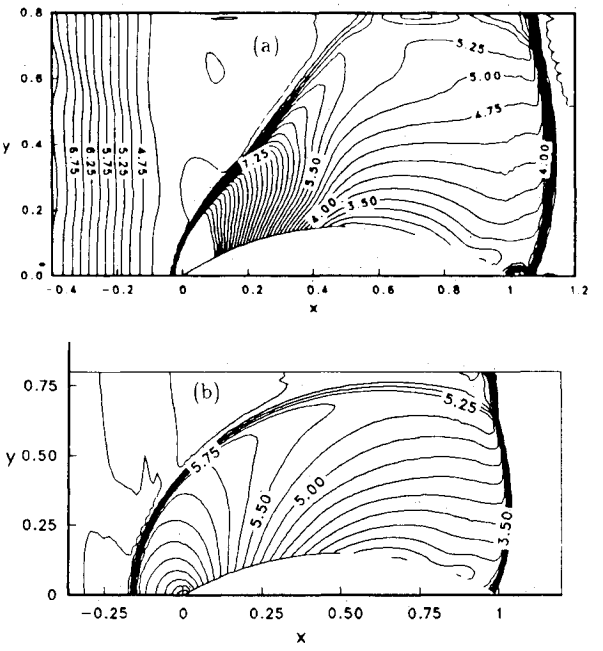

Fig. 3 Shock wave diffraction by a 15% circular arc model; pressure contours for $M_s = 2$ flow: a) starting with a diaphragm, b) starting with a single moving shock.

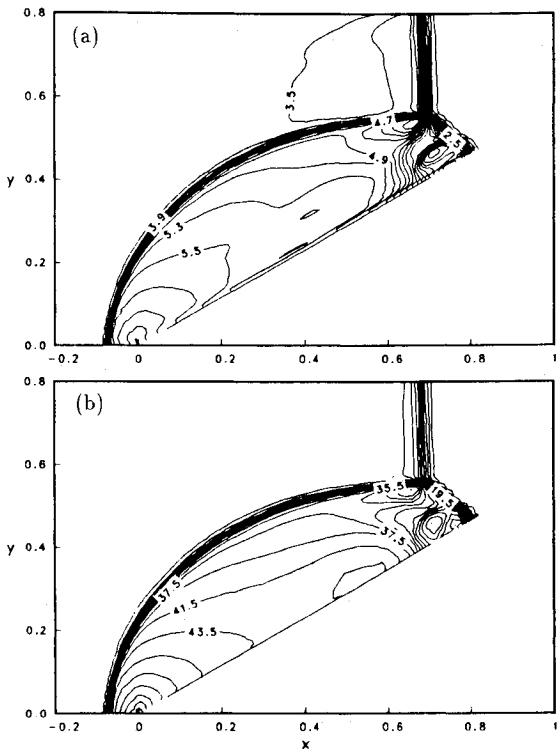

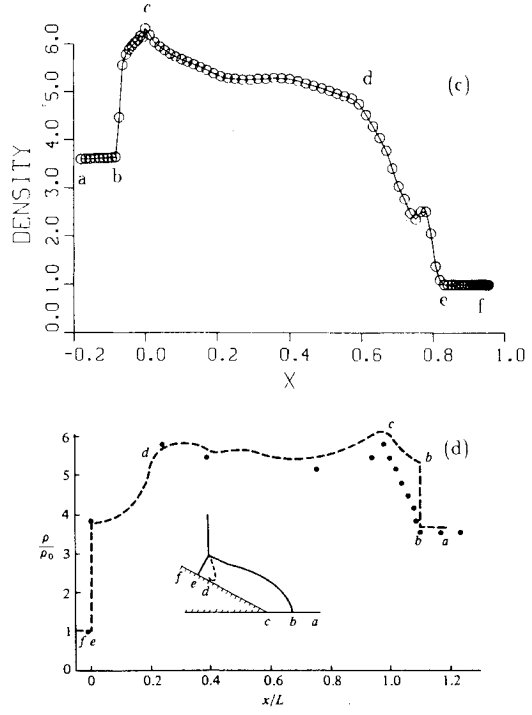

Fig. 4 Shock wave diffraction by a 30 deg compression wedge: a) isopycnics, b) pressure contours, c) density distribution on wedge surface, d) density distribution, experiments.[16,17]

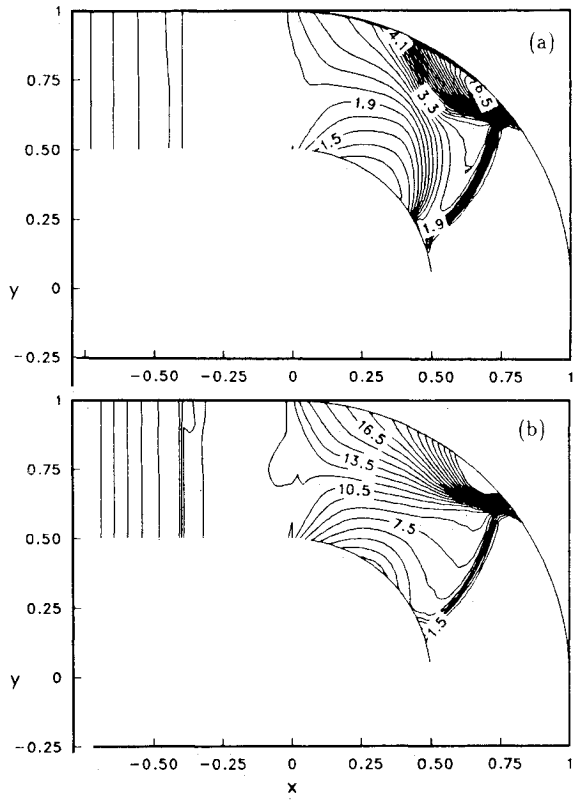

Fig. 5 Shock wave propagation along a 90° bent duct: a) isopycnics, b) pressure contours ($M_s = 6$).

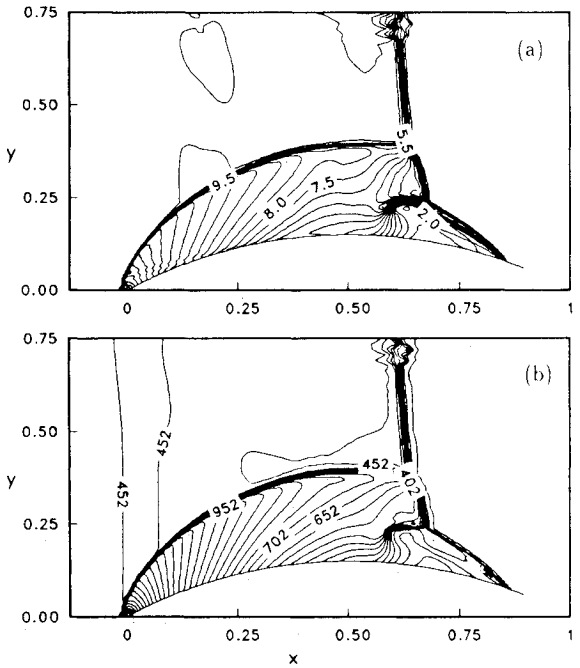

Fig. 6 Shock wave diffraction generated by a $M_s = 20$ flow passing a 15% thick circular arc model: a) isopycnics, b) pressure contours.

subjected to the diffraction and reflection process of shock waves and vortex generation behind them—important for determining the optimal configuration of the bend which would be capable of realizing stable shock transmission. Although the shock smears due to the coarse grids used, the general structures are well presented.

Finally, a shock moving with Mach number $M_s = 20$ impinging on the 15% circular arc model at two different times are shown in Fig. 6 and Fig. 7, respectively. The isopycnics, pressure contours, density distribution, and surface pressure distribution are shown. The incident shock I, reflected shock R, Mach shock T_1, T_2, vortex V, backward-facing recompression shock S_b, and the slip stream structures are well resolved. Interesting structures near the second triple point T_2 can be seen from the locally enlarged views. A fine grid of 201×101 was used to simulate this problem.

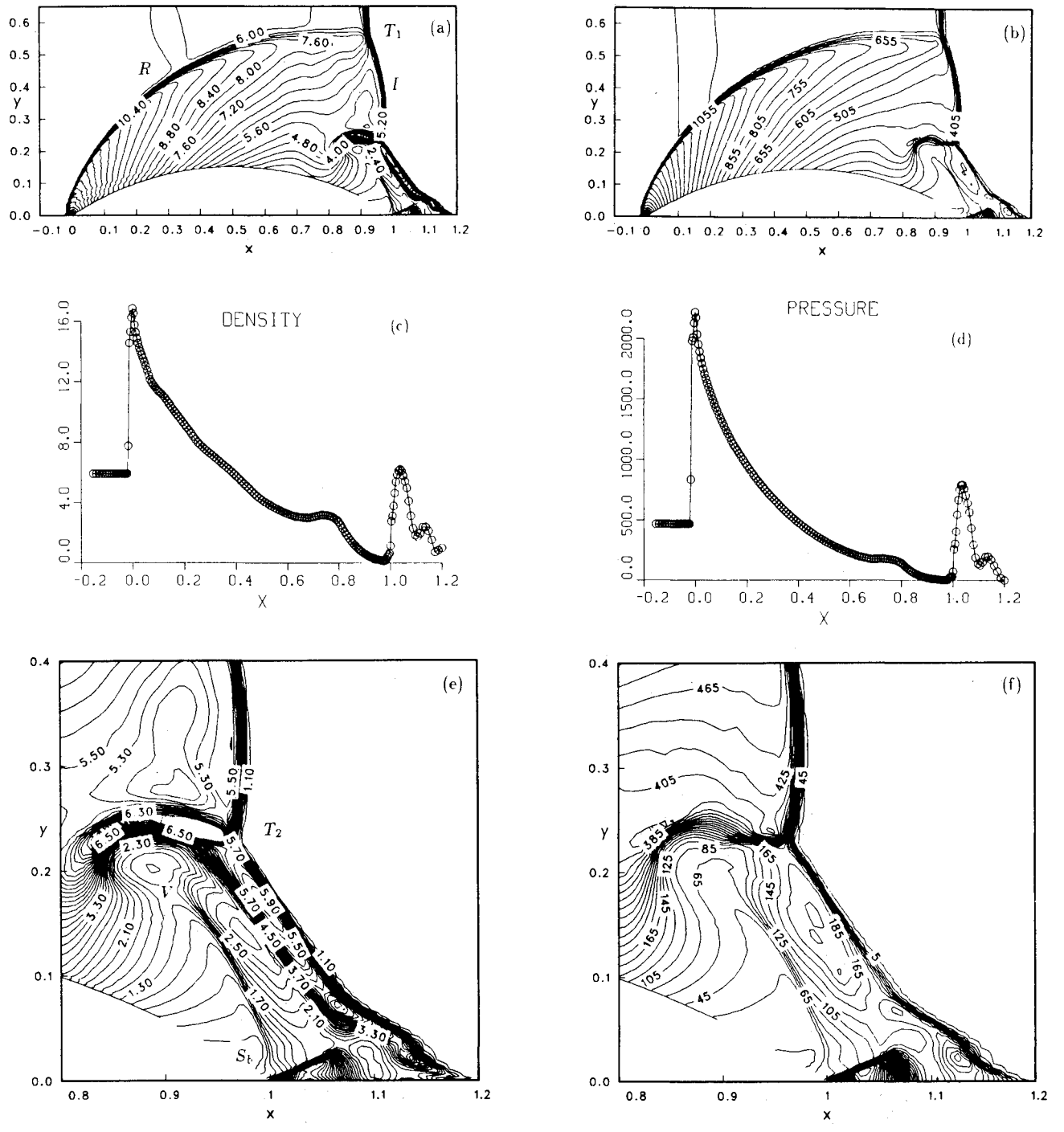

Fig. 7 Shock wave diffraction by a $M_s = 20$ flow passing a 15% thick circular arc model: a) isopycnics, b) pressure contours, c) density of a, f) enlarged view of b.

Conclusions

Two approaches to achieve second-order accuracy for the characteristic flux-difference splitting method have been described for solving the unsteady Euler equations, applied to the one- and two-dimensional transient shock tube flows. One approach is using a more accurate representation of the flux vectors similar to Harten's modified flux, and the other using a more accurate representation of the distribution of the conservative variables similar to van Leer's MUSCL approach. Numerical results for the one-dimensional shock tube problem indicates sharp resolution of discontinuities including shocks and contact surfaces. For multidimensional problems, the solution procedure is done through dimensional splitting, and the method is applied to simulate shock wave and object interaction for various geometries. A complex transient shock diffraction flow process for a broad range of shock Mach numbers were simulated. The numerical results are in good agreement with the experimental work and the present method is believed to be simpler to implement compared with the Godunov method. This study presents our first attempt to develop an unsteady Euler code for application to two-dimensional complex flows with a transient nature such as rotor aerodynamics, solid rocket ignition overpressure, or muzzle brake flowfields. Further enhancement of the resolution of the flowfields can be achieved by using solution-adaptive grid schemes.[18]

Acknowledgments

The first author thanks H. Lomax of NASA Ames Research Center for his support and encouragement throughout the

course of this study. This work was done under the auspices of the National Research Council.

References

[1]Harten, A., Lax, P., and van Leer, "Upstream Differencing and Godunov-Type Schemes for Hyperbolic Conservation Laws," *SIAM Review*, Vol. 25, 1983, pp. 35-61.

[2]Sweby, P., "High Resolution Schemes Using Flux Limiters for Hyperbolic Conservation Laws," *SIAM Journal of Numerical Analysis*, Vol. 21, No. 5, 1984, pp. 995-1011.

[3]Woodward, P.R. and Collela, P., "The Numerical Simulation of Two-Dimensional Fluid Flow with Strong Shocks," *Journal of Computational Physics*, Vol. 51, 1984, pp. 115-173.

[4]Lombard, C.K., Oliger, J., and Yang, J.Y., "A Natural Conservative Flux Difference Splitting for the Hyperbolic Systems of Gasdynamics" AIAA Paper 82-0976, 1982.

[5]Lombard, C.K., Oliger, J., Yang, J.Y., "A Natural Conservative Flux Difference Splitting for the Hyperbolic Systems of Gasdynamics," *Proceedings of the 8th International Conference on Numerical Methods in Fluid Dynamics, Springer Lecture Notes in Physics 141*, 1982.

[6]Yang, J.Y., "A Characteristic Flux Difference Splitting Method for Hyperbolic Systems of Conservation Laws," Ph.D. Dissertation, Stanford University, CA, March, 1983.

[7]Yang, J.Y., "Second- and Third-Order Upwind Difference Schemes for Hyperbolic Conservation Laws," NASA-TM-85959, July 1984.

[8]Yang, J.Y., "Numerical Solution of the Two Dimensional Euler Equations by Second-Order Upwind Difference Schemes," AIAA Paper 85-0292, 1985.

[9]Godunov, S.K., "A Difference Scheme for Numerical Computation of Discontinuous Solution of Hydrodynamic Equations," Mat-Sornik 47, 1959.

[10]Godunov, S.K., Zabrodin, A.V., and Prokopov, G.P., "A Computational Scheme for Two-Dimensional Nonstationary Problems of Gas Dynamics and Calculation of the Flow from a Shock Wave Approaching a Stationary State," *Zh. vych. mat. 1* No. 6, 1960, pp. 1020-1050.

[11]Harten, A., "High Resolution Schemes for Hyperbolic Conservation Laws," *Journal of Computational Physics*, Vol. 49, 1983, pp. 357-393.

[12]van Leer, B., "On the Relation between the Upwind-Difference Schemes of Godunov, Engquist-Osher, and Roe," ICASE Report 81-11, 1981.

[13]van Leer, B., "Towards the Ultimate Conservative Difference Scheme. V. A Second-Order Sequel to Godunov's Method," *Journal of Computational Physics*, Vol. 32, 1979, pp. 101-136.

[14]Anderson, W.K., Thomas, J.L., and van Leer, B., "A Comparison of Finite Volume Flux Vector Splittings for the Euler Equations," AIAA Paper 85-0122, 1985.

[15]God, G.A., "Survey of several Finite Difference Methods for Systems of Nonlinear Hyperbolic Conservation Laws," *Journal of Computational Physics*, Vol. 27, 1978, pp. 1-31.

[16]Ben-Dor, G. and Glass, I.I., "Domains and Boundaries of Nonstationary Oblique Shock-Wave Reflections. 2. Monatomic Gas," *Journal of Fluid Mechanics*, Vol. 96, 1980, pp. 735-756.

[17]Deschambault, R.L. and Glass, I.I., "An Update on Non-stationary Oblique Shock-Wave Reflections: Actual Isopycnics and Numerical Experiments," *Journal of Fluid Mechanics*, Vol. 131, 1982, pp. 27-57.

[18]Nakahashi, K and Deiwert, G.S., "A Practical Adaptive Grid Method for Complex Fluid Flow Problems," *Lecture Notes in Physics*, Vol. 218, 1984, pp. 422-426.